FULL PAPER

Highly Efficient and Stable Perovskite Solar Cells Based on Monolithically Grained $CH_3NH_3PbI_3$ Film

Chengbin Fei, Bo Li, Rong Zhang, Haoyu Fu, Jianjun Tian, and Guozhong Cao**

The synthesis and growth of perovskite films with controlled crystallinity and microstructure for highly efficient and stable solar cells is a critical issue. In this work, thiourea is introduced into the $CH_3NH_3PbI_3$ precursor with two-step sequential ethyl acetate (EA) interfacial processing. This is shown for the first time to grow compact microsized and monolithically grained perovskite films. X-ray diffraction patterns and infrared spectroscopy are used to prove that thiourea significantly impacts the perovskite crystallinity and morphology by forming the intermediate phase $MAI{\cdot}PbI_2{\cdot}S{=}C(NH_2)_2$. Afterward, the residual thiourea which coursed charge recombination is completely extracted by the sequential EA processing. The product has improved light harvesting, suppressed defect state, and enhanced charge separation and transport. The sequentially EA processed perovskite solar cells offer an impressive 18.46% power conversion efficiency and excellent stability in ambient air. More importantly, the EA postprocessed perovskite solar cells also have excellent voltage response under ultraweak light (0.05% sun) with promising utility in photodetectors and photoelectric sensors.

1. Introduction

The rapid emergence of hybrid organic–inorganic perovskite solar cells has received tremendous interest in the photovoltaic field due to cost-effective processing, strong light absorption and low nonradiative carrier recombination rates.[1,2] Within the unremitting efforts of many researchers worldwide in recent years, the solar-to-electrical energy conversion efficiency of perovskite solar cells has been dramatically improved to 22.1% under 1 sun illumination.[3] To obtain stable and reproducible high performance device, several factors that have pivotal impacts on the perovskite films are under intense study including the crystallization behavior, the deposition method, and the reactant components.[4,5]

Several strategies have been studied to enhance the crystallinity and surface morphology of the active layer via the composition of the perovskite precursors. By replacing the lead precursor PbI_2 with $PbCl_2$ or $Pb(CH_3COO)_2$, the morphology of perovskite film and the device stability were strongly influenced due to decelerated crystallization kinetics and selected crystallographic orientation.[6,7] For the organic iodine precursor, methylammonium iodide (MAI) combined with methylammonium bromine or formamidine iodide (FAI) showed notable changes on energy bandgap, thermal or moisture stability, grain size, and ion migration behaviors. This was mainly due to the variation of relative ion sizes and lattice structure.[8] Besides the selection on lead and organic iodine precursors, some ligand compounds that act as electron donor (Lewis-bases) could also greatly affect the properties of perovskite films.[9]

Three categories of Lewis-bases can coordinate with PbI_2 and promote the sequential deposition of perovskite film: O-donor, N-donor, and S-donor.[10] Dimethylsulfoxide (DMSO), is an O-donor, and has received much attention for having successfully grown uniform and dense perovskite films due to the formation of immediate phase $MAI{\cdot}PbI_2{\cdot}DMSO$, which retarded the otherwise rapid reaction between PbI_2 and organic iodide in solution.[11] Furthermore, an intramolecular exchange process between DMSO and FAI was also reported to fabricate $FAPbI_3$ with a flat and dense surface without volume expansion.[12] However, due to the weak coordination between O and Pb, the O-donor was easy to escape from the PbI_2 framework. This often leads to insufficient perovskite grain growth. Perovskite films with smooth surfaces and large grains are desired with effective photon capture, fast carrier transport, and suppressed ion migration.[13] Thus, more stable ligands are needed for the fabrication of perovskite films.

A new perovskite precursor and a two-step antisolvent processing method were utilized to grow high-quality perovskite films. By introducing thiourea into the pristine $CH_3NH_3PbI_3$ precursor in equivalent molar ratios, the perovskite films acquired the desired morphology. Sequential ethyl acetate (EA) antisolvent processing removed the residual thiourea and opened the grain

Dr. C. Fei, R. Zhang, Dr. H. Fu, Prof. G. Cao
Beijing Institute of Nanoenergy and Nanosystems
Chinese Academy of Sciences
National Center for Nanoscience
and Technology (NCNST)
Beijing 100083, China
E-mail: gzcao@u.washington.edu
Dr. B. Li, Prof. J. Tian
Advanced Material and Technology Institute
University of Science and Technology
Beijing 100083, China
E-mail: tianjianjun@mater.ustb.edu.cn
Prof. G. Cao
Department of Materials and Engineering
University of Washington
Seattle, WA 98195-2120, USA

DOI: 10.1002/aenm.201602017

boundaries to form monolithic perovskite grains. Such processed perovskite films that possess enhanced light absorption, suppressed surface defect, and accelerated charge separation and transport; the power conversion efficiency of the solar cells based on such perovskite films reached 18.46% with much enhanced stability and repeatability. An excellent voltage response was also observed under ultraweak light illumination, potentially for photodetector and photoelectric sensor applications.

2. Results and Discussion

Figure 1a is a schematic diagram of the deposition of perovskite materials by an antisolvent precipitation and sequential solution postprocessing. A mixture of MAI, PbI_2, and thiourea of equivalent molar ratios was first spread over the entire substrate of FTO (F-doped SnO_2)/50 nm TiO_2 compact layer/100 nm TiO_2 mesoporous layer. Afterward, two-step EA processing was utilized to fabricate pure phase perovskite films. During spinning, the antisolvent EA was dripped on the substrate to extract the original solution dimethylformamide (DMF) to ensure fast crystallization of perovskite intermediate phase. Then, the as-prepared film was covered with additional EA solution (EA postprocessing without spinning). This remained for 60 s to remove the residual reacted thiourea. Finally, highly uniform crystalline perovskite was obtained via heating at 90 °C for 30 min.

As shown in Figure 1b, the pristine perovskite film (without thiourea containing precursor and EA postprocessing) exhibited

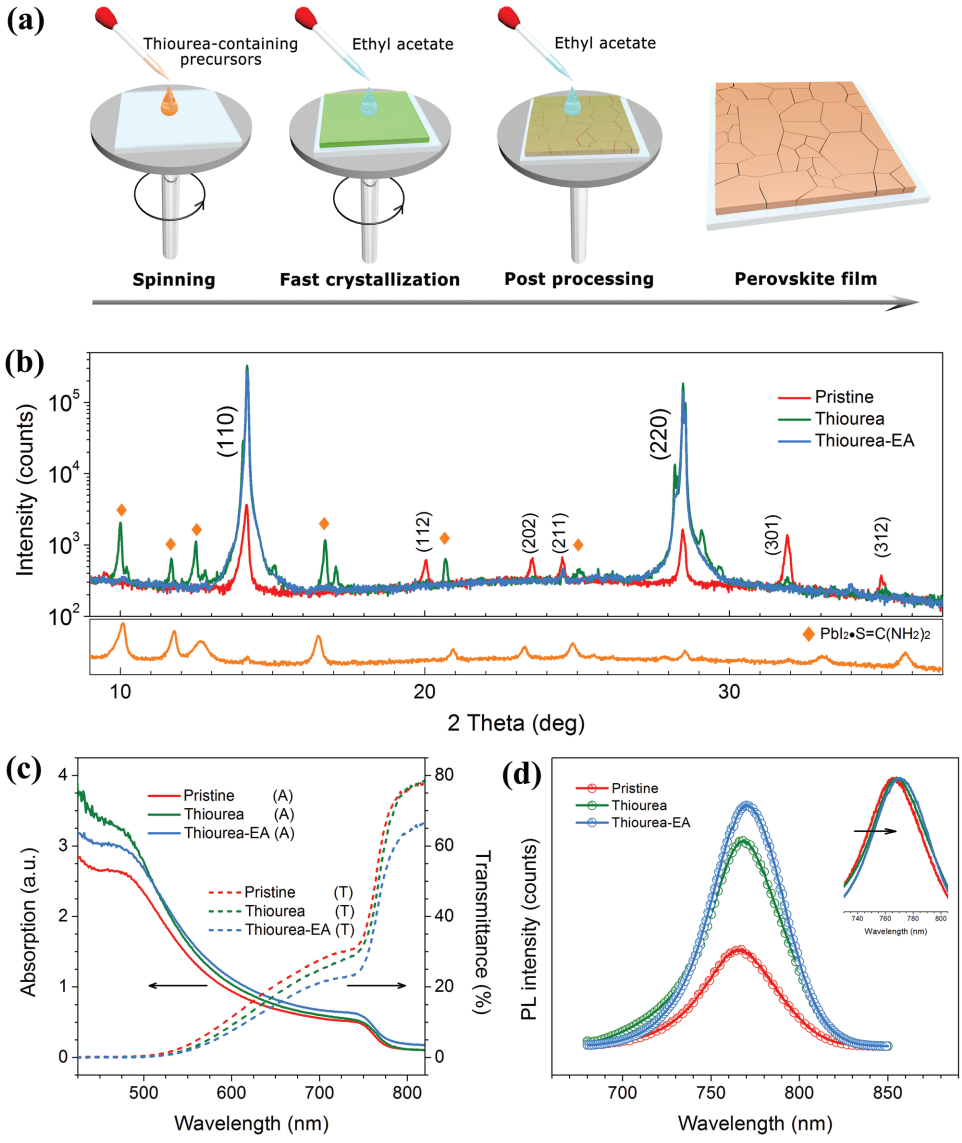

Figure 1. a) Schematically fabrication process of perovskite films with thiourea-containing precursor and ethyl acetate postprocessing. b) The XRD patterns of perovskite fabricated under different conditions. All the perovskite films were prepared on the FTO substrates. The intensity of the vertical axis is indexed to give the weak peaks higher recognition. c) UV–vis measurement for the three perovskite films—the solid line and the dashed line represent absorption and transmittance curve, respectively. The FTO substrate was used as the baseline. d) The steady-state photoluminescence curves emitted at 775 nm and were obtained for the perovskite films upon excitation at 445 nm. The inset showed the relative PL intensities of the perovskite films.

typical diffraction peaks of solution-processed perovskite $MAPbI_3$, including several weak peaks and two notable characteristic peaks at 14.2° and 28.4° that correspond to (110) and (220), respectively.[14] By introducing thiourea to the perovskite precursor, the crystallinity of the perovskite films was significantly improved, and the intensity of the peaks were nearly two orders of magnitude higher than that of the pristine film. The full width at half maxima (FWHM) of the (110) plane was also reduced from 0.14° to 0.07°, suggesting increased crystallite size and decreased bulk defect.[15] The weak peaks of perovskite were almost invisible, indicating that the crystallographic orientation, especially the (110) plane, was strongly induced by the presence of thiourea. Such an oriented crystal growth was conducive to the formation of micrometer-sized perovskite grains with limited thickness (typically 400–500 nm).[16] Several minor peaks were found in the X-ray diffraction (XRD) pattern. There were identified to be the intermediate phase $PbI_2{\cdot}S{=}C(NH_2)_2$ in the inset. After the sequential EA treatment, those peaks disappeared completely confirming that EA is a powerful extracting agent to remove the residual thiourea. Because there was no variation in the position and FWHM of diffraction peaks of perovskite with and without EA processing, the thiourea likely resided mainly at the surface and/or grain boundaries instead of being inserted into the crystal structure.

The ultraviolet–visible (UV–vis) spectrum and steady-state photoluminescence (PL) curves were measured to further understand the effect of thiourea and EA postprocessing on the optical properties of perovskite films. When compared with the pristine film, the film prepared from thiourea containing precursor showed stronger absorption at the full light absorption range (Figure 1c). This was attributed to the increased crystallinity, enlarged grain size, and possibly reduced reflection.[17] With the sequential EA processing, the light absorption at the wavelength above 510 nm significantly enhanced, which was mainly due to the reduced surface defects from the intermediate phase $PbI_2{\cdot}S{=}C(NH_2)_2$, while the decreased absorption at the short wavelength (below 510 nm) was caused by the reduced photon capture of narrow bandgap intermediate phase (see Figure S2, Supporting Information). Moreover, the absorption edge was slightly red-shifted which revealed a narrowed bandgap and better energy level distribution to ensure that the low energy photons can be captured by perovskite. The transmittance was also measured to better identify the light-absorption capacity of perovskite materials. Unlike the complicated absorption features, perovskite with sequential postprocessing showed reduced transmittance at the long-wavelength range and almost extinction at the short-wavelength range, as a result of enhanced light harvesting efficiency.

To assess the emission properties of the $MAPbI_3$ crystal, a quenched steady-state PL spectroscopy study was done (Figure 1d). All samples were prepared on the plasma cleaned glasses to avoid the influence of charge injection among the active layer and electron transfer materials. The perovskite emission peak intensities were found to increase upon addition of thiourea precursor and EA postprocessing, while the FWHM was slightly narrowed for the final product, which indicated the reduced surface defect and enhanced crystallinity. The typical Stokes shifts centered at ≈770 nm were also observed for all the emission peaks, which was in a good agreement with the literature.[18] Corresponding to the above absorption result, the emission peak positions of the samples with extra variations on precursor and processing were red-shifted by 3 and 5 nm, which revealed the adjustment of energy level dispersion.

With the new perovskite precursor and EA postprocessing, highly crystallized, large grained, and pinhole-free $MAPbI_3$ films were produced. **Figure 2**a–f showed the top-view scanning electron microscopy (SEM) images of the perovskite films prepared from three different conditions. The crystal grain size increases substantially from 500 nm to over 2 μm, confirmed that thiourea in the precursor has exerted a crucial impact on the nucleation and subsequent crystal growth processes. With the EA postprocessing, grain boundaries blocked by the intermediate phase were opened (Figure 2e,f) resulting in a subtle decrease in grain size. Interestingly, the rough and striped microstructure that covered the perovskite surface (the insets) also disappeared after the solution treatment, which was in principal coursed by the interfacial extraction of thiourea. Since the rough surface and intensive grain boundaries were reported as the most efficient routes for ion migration, the smooth and large grained perovskite obtained from the postprocessing was promising to provide high efficiency perovskite solar cells with less hysteresis.[13]

Given that the opened grain boundary might lead to charge leakage between the infiltrated hole transfer material and the electron transfer material, the bottom image of perovskite film peeled from FTO substance was also characterized in Figure 2g. The grains at the bottom area of the perovskite layer were almost linked together, but no apparent gaps were observed. This guaranteed valid charge transport in the device. As illustrated in the cross-sectional SEM images in Figure 2h, the solar cell was stacked in the structural sequence of FTO/compact TiO_2/mesoporous TiO_2 and perovskite/perovskite capping layer/spiro-OMeTAD/Au electrode. The thickness of the perovskite capping layer was ≈400 nm, and this was reported as the most suitable thickness for both photon capturing and carrier transport.[19] More importantly, highly uniform, monolithic perovskite grains were observed in the capping layer, which was beneficial to the longitudinal electron transport.[20]

The dark brown $MAPbI_3$ films B_1 and B_3 shown in **Figure 3**b were obtained from Figure 3a after 30 min heat processing, while B_2 was formed by the first-step EA processing for the fast crystallization versus the 3 min thermal treatment on the light green transparent film (A_2). Unlike the pristine precursor, the thiourea-containing precursor does not suffer from the "sixth second" problem (only the sixth second was appropriate for the film fabrication in the conventional antisolvent method).[21] This ensured longer operating time and good repeatability. An infrared (IR) spectroscopic study was conducted to clearly investigate how thiourea works in the perovskite formation process. Figure 3c showed IR spectra for the DMF solution with PbI_2, thiourea, PbI_2·thiourea and MAI + PbI_2+thiourea. The C=S stretching vibration was observed at 743 cm^{-1} for pure thiourea, which was shifted to 717 cm^{-1} for the compound phase PbI_2·thiourea. This was further shifted to 721 cm^{-1} for the thiourea-containing precursor (see Figure 3d). When PbI_2 was combined with thiourea, the force constant of C=S decreased due to partial electron cloud migration from C=S to S·Pb, which led to the decline of stretching vibration frequency because the

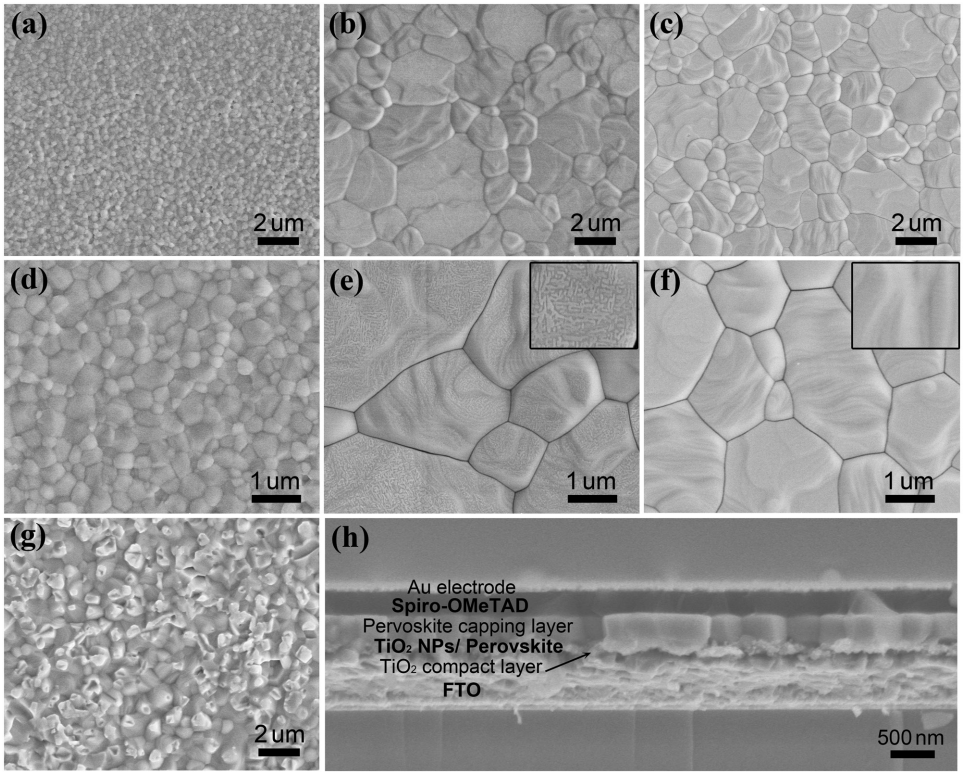

Figure 2. SEM images of perovskite films prepared from different conditions: a,d) with pristine perovskite precursor, b,e) with thiourea-containing perovskite precursor, c,f) with thiourea-containing perovskite precursor and EA postprocessing. g) Bottom image shows the "thiourea-EA" perovskite film peeled from the FTO substrate. h) Cross-section image of the perovskite solar cells fabricated with thiourea containing precursor and ethyl acetate postprocessing. The insets in (e) and (f) showed high-resolution images of the perovskite films.

frequency was proportional to the square root of force constant in the diatomic harmonic motion model.[22] We noted that the wavenumber of C=S stretching in the thiourea-containing precursor was lower than that of the PbI_2·thiourea, which revealed the variation of electron density with the competitive effect of MAI·Pb and $(NH_2)_2C{=}S{\cdot}Pb$. Because there were no obvious shifts on the peak positions of H−I stretching and N−H bending for the mixture with and without thiourea (Figure S3, Supporting Information), thiourea was unlikely to combine with MAI in the mixture, and this further verified the precursor format to be $MAI{\cdot}PbI_2{\cdot}S{=}C(NH_2)_2$.

With the above optical, crystallographic and morphology analyses, the main chemical reactions involved in the formation process of monolithic perovskite grains can now be proposed. Figure 3e and Figure S4a (Supporting Information) show that the reactants PbI_2, MAI, and thiourea were first dissolved in DMF solution and combined into the precursor $MAI{\cdot}PbI_2{\cdot}S{=}C(NH_2)_2$, while transparent and light yellow mixture was obtained at ambient condition. During the spin deposition, the antisolvent EA accelerated the perovskite crystallization from the original solution DMF. The EA postprocessing was used to sequentially extract the residual thiourea that covered the perovskite surface or inserted in the grain boundary. Surprisingly, thiourea was insoluble in EA but was extracted in postprocessing, which was attributed to the coordinated DMF that had been ignored. In light of the fact that thiourea cannot be entirely dispersed into the extracting agent until the DMF molar come to twofold of thiourea (Figure S4b, Supporting Information), the existing form of thiourea should be $S{=}C(NH_2)_2{\cdot}2DMF$. This provided an adequate driving force for the dissolution of thiourea in EA solution.

The intermediate phase that formed at the interface of perovskite grains was initially $PbI_2{\cdot}S{=}C(NH_2)_2{\cdot}2DMF$, which then transferred into $PbI_2{\cdot}S{=}C(NH_2)_2$ under additional thermal treatment. With sequential EA surface treatment, DMF was rapidly mixed with EA under the driving force of the solvent polarity.[23] This resulted in the extraction of $S{=}C(NH_2)_2$ due to the hydrogen bonding between $S{=}C(NH_2)_2$ and DMF molecules (Figure S5, Supporting Information). However, the intermediate phase was found to remain in the perovskite film with nonsequential processing (the film was annealed for 3 min to remove the combined DMF before surface processing; Figure S6, Supporting Information). These data suggested the importance of continuity in the postprocessing and also incidentally confirmed the present of $S{=}C(NH_2)_2{\cdot}2DMF$. Finally, monolithic perovskite grains were formed with opened grain boundaries, which were believed to benefit the interfacial contact of hole transfer material (HTM) and perovskite. Consequently, interface charge separation was improved.

Figure 4a demonstrates the photovoltaic performance of the perovskite solar cells that were prepared under three different conditions. The detailed performance parameters are summarized and listed in **Table 1**. Versus the solar cells fabricated from the pristine condition, the device

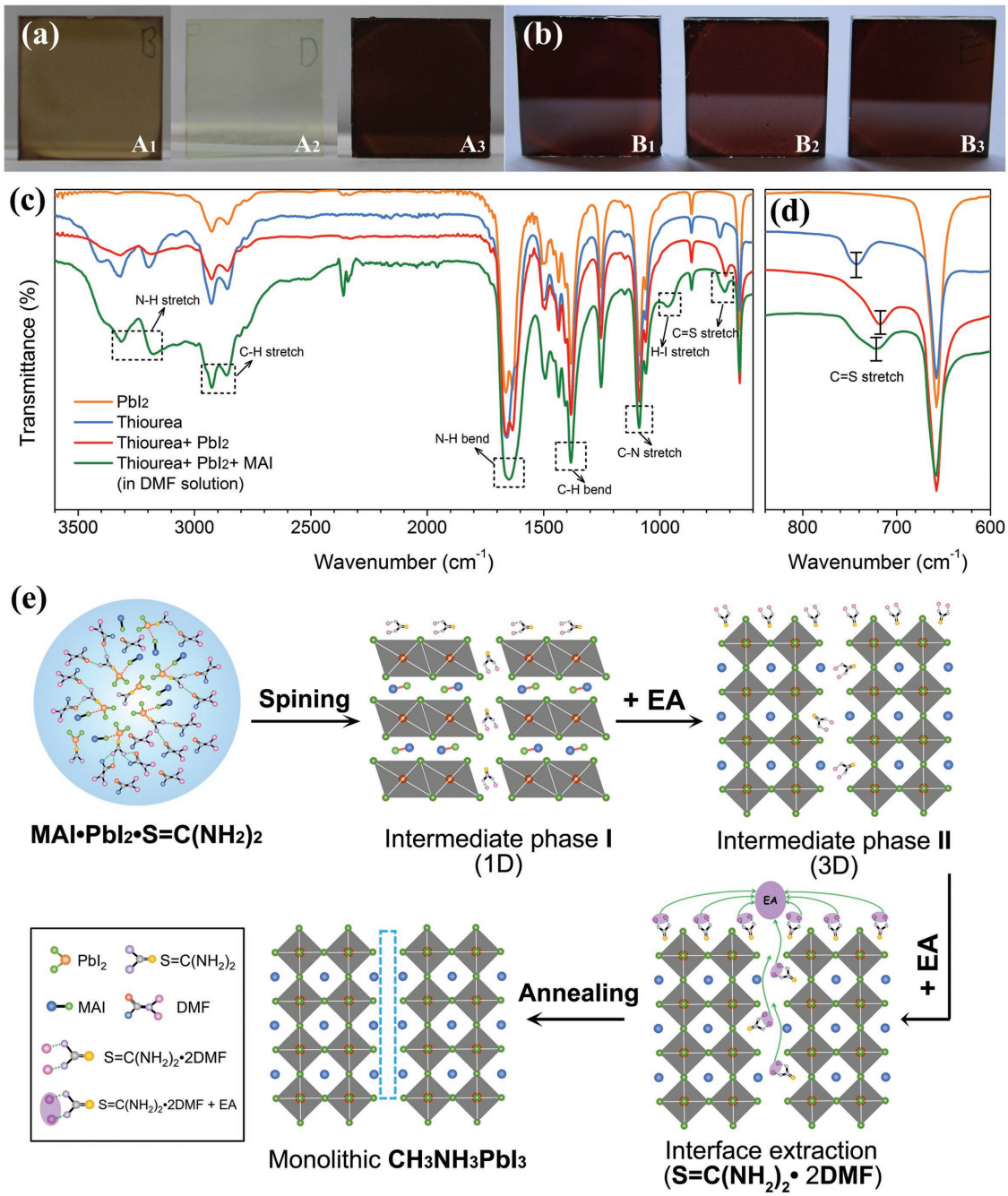

Figure 3. Photographs of the film a) before and b) after heating processing: A_1 (B_1), A_2 (B_2), and A_3 (B_3) represent the pristine films, thiourea-induced films, and sequential EA processed films, respectively. Infrared spectroscopy of the perovskite precursors in c) full scanning range and d) selected fingerprint identification zone. e) Schematic reaction process from the precursor to monolithic perovskite grains.

with thiourea-containing precursor and EA postprocessing obtained higher short-circuit current density (J_{SC}), which increased from 20.86 to 22.49 mA cm^{-2}. This was mainly due to better light absorption and charge transportation. Open-circuit voltage (V_{OC}) was greatly affected by the relative position of quasi-Fermi level in the contacted perovskite and electron transfer material (ETM) as well as the defect-induced recombination in the electron transport channels.[24] Perovskite films with large sized grains and fewer surface defects had a lower conduction band position. This was beneficial to the band alignment of perovskite and ETM.[25,26] With the enlarged grains and reduced surface defect, the V_{OC} was significantly increased in the sequentially processed perovskite solar cells. The fill factor (FF) was the third parameter that determined the power conversion efficiency of perovskite solar cells, and this was restricted by the complex energy losses from the electrode surface reflection, series resistance, and shunt resistance.[27]

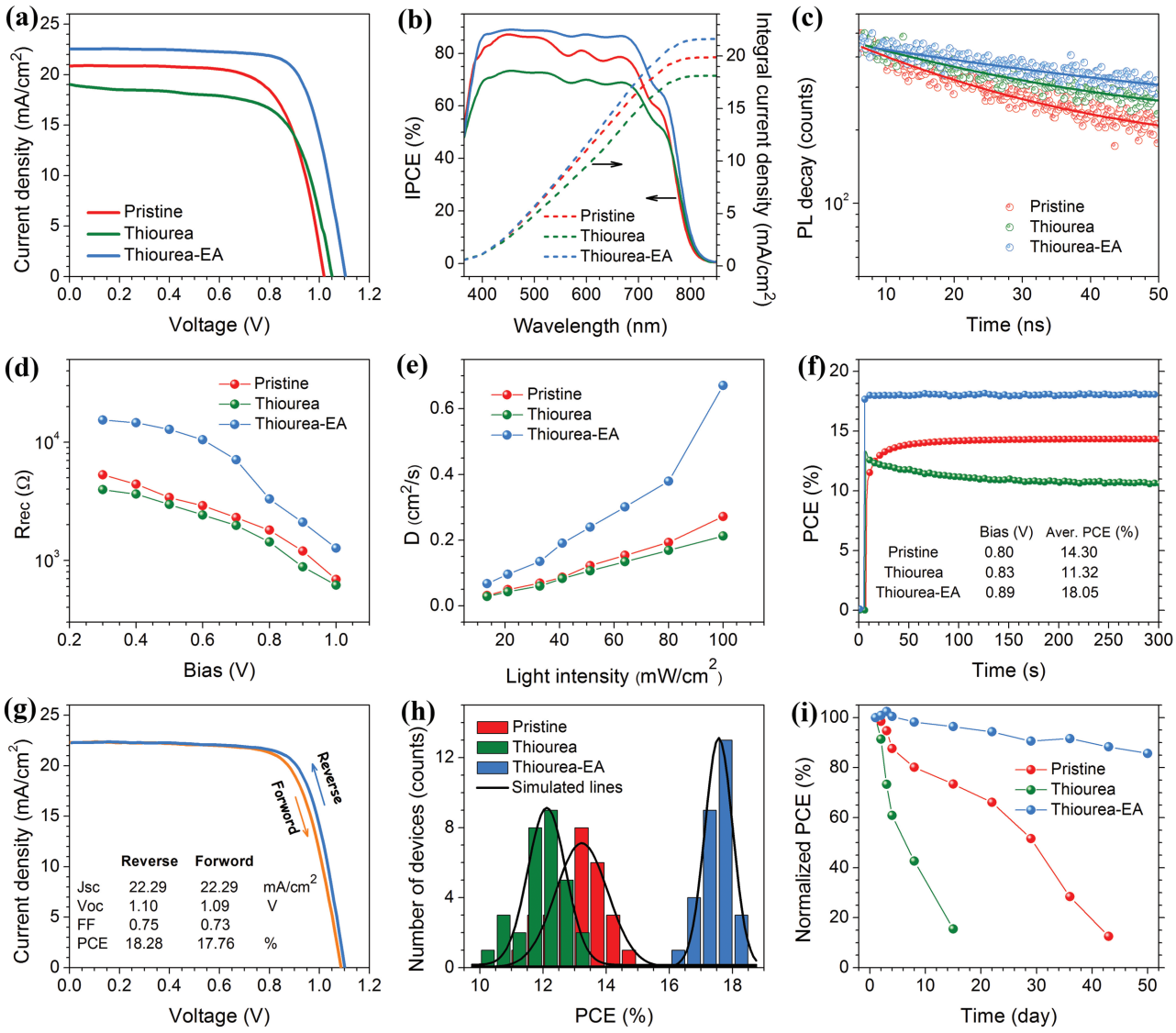

Figure 4. a) The current density–voltage curves of perovskite solar cells fabricated by different methods. b) Internal photo-to-current efficiency measurement and the corresponding integral current density for the devices fabricated from different precursors. c) The time-solved photoluminescence decay at 775 nm obtained for the perovskite films upon excitation at 445 nm. d) Recombination resistance of the solar cells under different biases. e) Diffusion coefficient of solar cells at different working voltages of the light source. f) Steady power conversion efficiency curves of solar cells fabricated under different conditions (the average PCE is calculated from 100 to 300 s). g) Current density–voltage curve of the sequential processed perovskite solar cells with different scanning directions. The scanning range is –0.1 to 1.2 V, while the scanning rate is 10 mV s^{-1}. h) Statistical PCE for the perovskite solar cells (from 30 samples for each condition). i) Long-term stability of solar cells for 50 d. All devices were stored in the dark in ambient air (humidity: 10%–50%, temperature: 10–25 °C).

Table 1. Parameters of current density–voltage curves and steady-state PL obtained from perovskite solar cells when fabricated under different conditions.

PSCs	J_{sc} [mA cm^{-2}]	V_{oc} [V]	FF	PCE [%]	Average PCE [%]	τ_1 [ns]	τ_2 [ns]
Pristine	20.86	1.02	0.69	14.75	13.22 ± 1.94	1.67	24.60
Thiourea	19.04	1.05	0.67	13.38	12.12 ± 1.41	2.11	32.48
Thiourea-EA	22.49	1.10	0.75	18.46	17.57 ± 1.03	1.02	54.68

With sequential postprocessing, the series resistance was reduced by the increased crystallinity and enlarged monolithic grains, while the shunt resistance increased by the reduced bulk and surface defects, leading to improved FF from 0.69 to 0.76. The overall photovoltaic performance was greatly elevated from 14.75% to an impressive efficiency 18.46% for the champion solar cells. However, the solar cells with thiourea precursor and without sequential surface processing presented both diminished J_{SC} and FF and mediocre V_{OC}. This resulted from the blocked charge transport[28] and serious charge recombination[29] produced by the intermediate phase $PbI_2{\cdot}S{=}C(NH_2)_2$.

To understand the origin of these variations in solar cells performance, several photoelectric and electrochemistry experiments were performed. Figure 4b shows that the internal photo-to-current efficiency spectrum (IPCE) of the solar cells investigated the changes in J_{SC}. A broad IPCE plateau of over 85% between 400 and 700 nm was observed for the EA sequential processed device. The integrated current density corresponding to J_{SC} was calculated to be 19.88, 18.14, and 21.63 mA cm^{-2} for the three solar cells, respectively. These were quite consistent with the current density obtained from the J–V curves.

Trap states were typically observed in perovskite, and these have serious negative impacts on photovoltaic performance.[30] The trap states were likely caused by electron–phonon coupling, which strengthened the positions where the crystal structure was most susceptible to deformation.[31] A time-resolved PL technique was employed to check trap state density in the active layers, which were fabricated under different conditions (Figure 4c). The spectra of the perovskite films on the TiO_2 nanoparticle coated glass monitored at the peak emission (770 nm) could be fitted to biexponential decays with a fast component τ_1 and a slow component τ_2, while the detailed fit data are listed in Table 1. The fast decay component could be assigned to the interfacial charge separation property, while the slow component corresponded to a nonradiative recombination property of the bulk materials.[32] The faster τ_1 and slower τ_2 of fluorescence decay for the sequential processed perovskite layer attested to the suppressed nonradiative recombination induced by the trap state. This promoted interfacial charge separation, resulting from the higher crystal quality of the monolithic perovskite grains.

The fast component τ_1 of the perovskite films both approached 1 ns, which is the detection limit of PL decay. Thus, electrochemical impedance spectroscopy (EIS) and intensity modulated photocurrent/photovoltage spectroscopy (IMPS/IMVS) were utilized to monitor the interfacial properties of the perovskite solar cell system. The recombination resistance (R_{rec}) in the simulated equivalent circuit (Figure S8, Supporting Information) consisted of the interfacial resistances of perovskite/electron selective layer (ETL) and perovskite/HTM.[33,34] As reported in the literature,[35] $\frac{\mathrm{d}\lg(R_{rec})}{\mathrm{d}V} = \frac{q}{2.303nk_BT}$, $\lg(R_{rec})$ was inversely proportional to the applied voltage (Figure 4d). The enhanced recombination resistance of the sequential processed perovskite solar cells revealed reduced surface defect states and thus reduced charge leakage, leading to significantly improved FF and V_{OC}. Similar to R_{rec}, the carrier diffusion coefficient (Figure 4e) determined from the IMPS/IMVS spectra was doubled for the sequential processed solar cell. Therefore, the overall photovoltaic performance of the sequential processed solar cells was notably improved including the enhanced light harvesting, accelerated electron transport and separation, and reduced defects.

The perovskite solar cells with different durations of EA postprocessing and different thiourea concentrates were also investigated. According to the XRD patterns shown in Figure S9 (Supporting Information), the thiourea was not entirely extracted by EA postprocessing until 60 s. While longer processing times might lead to unexpected chemical corrosion on the crystal surface, the perovskite film with 60 s EA treatment exhibited better light absorption at the long-wavelength range (Figure S10, Supporting Information). Figure S11 (Supporting Information) shows that the photovoltaic performance first increased with prolonged processing time and then slightly declined at times over 60 s. In addition, the devices prepared from the perovskite precursor with equimolar equivalents of thiourea demonstrated the best performance (Figure S12 and Table S2, Supporting Information).

To further confirm the reliability of the solar cells prepared via different fabrication conditions, the steady-state power conversion efficiency (PCE) was measured under constant bias that equals to the voltage of the maximum power point[36] (Figure 4f). An average PCE of 18.05% was seen for the sequentially processed solar cell.

Hysteresis was an important issue in estimating the actual PCE,[37] and thus the current density–voltage curves of the sequential processed solar cell were also collected with the forward and the reverse directions (Figure 4g). The results summarized in the inset show that the device with large and monolithic grains had 0.52% PCE hysteresis, this is lower than most of $MAPbI_3$-based perovskite solar cells as reported in the literature.[38,39] The hysteresis was shown to be caused by the migration of MA^+ and I^- along the crystal surface and grain boundaries. This was inherent property of the material that was difficult to completely eliminate.[40] Moreover, the statistic PCE histogram of the solar cells along with the Gaussian fitting[41] was also illustrated in Figure 4h. For the EA sequentially processed solar cells, it had an impressive average PCE of 17.57 ± 1.03% over 30 devices, which demonstrated the outstanding reproducibility.

Long-term stability is one of the most critical challenges of perovskite solar cells from the transition stage to practical applications.[42] The PCE of the fabricated solar cells as a function of storage time is presented in Figure 4i. Clearly, the sequentially processed solar cell had excellent stability against erosion in the ambient air. After 50 d of storage, the solar cells based on perovskite films with EA postprocessing retained over 85% of the initial PCE, while the pristine solar cells lowered to less than 20% in 43 d. Such superb ambient air stability could be attributed to the monolithically grained morphology, high crystallinity, and decreased surface defects. This lessened the vulnerable sites when exposed in humid air.[33,43] The fast degradation of the thiourea assisted perovskite solar cell was resulted from the numerous surface defects introduced by the intermediate phase.

Perovskite is useful in other optoelectronic devices including photodetectors and photoelectric sensor because of its high extinction coefficient, long carrier lifetime, and diffusion length.[44] To investigate the light responsiveness of the perovskite films with monolithic grains, the steady-state photogenerated voltage was monitored with constant incident light intensity. As shown in **Figure 5**a, the sequentially processed solar cell exhibited stable voltage output, which was comparable to the inorganic silicon solar cell. Due to the possible photodegradation and ion migration behavior in the active layer, the voltage of the pristine solar cell slightly declined over time.

Figure 5b demonstrated the dependence of V_{OC} on the illuminated light intensity φ. To avoid the influence of trap states under a weak light illumination, the simulated lines were fitted

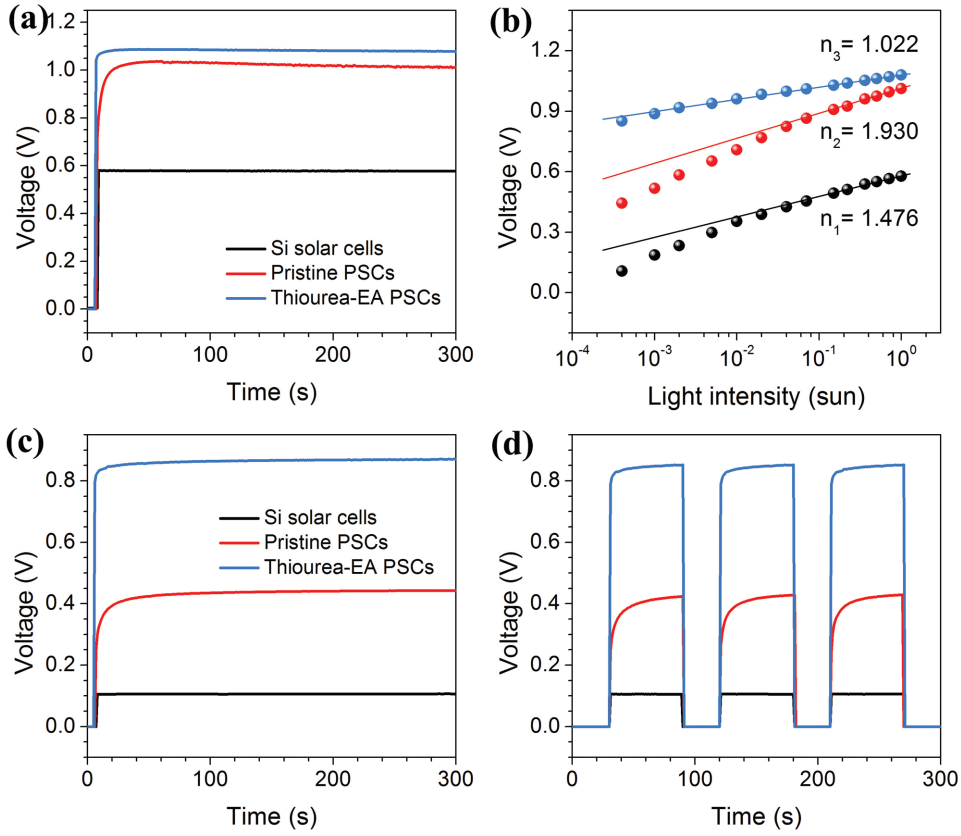

Figure 5. a) The steady-state open-circuit voltage curve under 1 sun light illumination. b) The open-circuit voltages under different illuminate intensities. Voltage response curve under 0.05% sun illumination for c) continuous light and d) intermittent light.

from the light intensities higher than 0.1 sun. The diode ideality factor, n, was commonly used to describe the dependence of applied light intensity and voltage.[45] This was defined as $n = \frac{q}{2.303 k_B T} \cdot \frac{dV_{oc}}{dlg(\varphi)}$. In theory, n could take different values between 1 and 3, depending on the recombination mechanism. The fitted values of light ideality factor were both located at 1–2, which indicated Shockley–Read–Hall trap-assisted recombination.[46] The sequentially processed perovskite with n_3 = 1.022 specified the recombination was limited by minority carrier, while the recombination in the pristine perovskite was limited by both types carrier with n_2 = 1.930.[35]

Figure 5c,d presented and compared the steady-state voltage response of the three devices under ultraweak light illumination (0.05% sun). The sequentially processed perovskite solar cell showed 0.86 V voltage output, which was much higher than that of the other two devices. This offered highly recognizable voltage signal for the applications in photodetectors and photoelectric sensors. As the light intensity decreased to values unrecognized by silicon solar cell (much lower than 0.01% sun), there was still remarkable voltage signal from the sequentially processed solar cell (Figure S12, Supporting Information). Collectively, the large, smooth, and monolithic $CH_3NH_3PbI_3$ was promising in applications for ultraweak light detection and recognition.

3. Conclusion

A novel perovskite precursor and two-step interfacial processing method was developed to synthesize $CH_3NH_3PbI_3$ films. By introducing thiourea to the perovskite precursor, the crystallization process was effectively controlled, while compact, smooth, and large grained perovskite films were achieved. This enhanced crystallinity and enlarged grains, improved the light harvesting of thiourea-induced perovskite films across the absorption range. However, an intermediate phase $PbI_2{\cdot}S{=}C(NH_2)_2$ was formed by the residual thiourea. This increased the interface recombination and further diminished the photovoltaic performance. With sequential postprocessing, the intermediate phase $S{=}C(NH_2)_2{\cdot}2DMF$ on the perovskite surface and at the grain boundaries was completely extracted by the robust hydrogen bonds between DMF and EA solution. The monolithic grains with open grain boundaries enhanced the contact between monolithic perovskite grains and hole transfer materials. This led to faster charge separation at the interface. The electron transport was significantly improved because the surface defect states were reduced by the sequential postprocessing. The resulting perovskite solar cells with sequential processing demonstrated an impressive power conversion efficiency of 18.46% and an average steady-state PCE of 18.05%. With the thiourea-containing precursor and sequential

EA processing, the device reproducibility and stability were also greatly improved. More importantly, an excellent voltage responsiveness was also observed for the sequentially processed perovskite solar cells under ultraweak light illumination (0.05% sun). This suggests the promising applications in photodetectors and photoelectric sensors.

4. Experimental Section

Device Fabrication: TiO_2 compact layer was deposited on clean FTO substrates with a magnetron sputtering apparatus, while annealed in air at 450 °C for 0.5 h. Afterward, the TiO_2 nanoparticle (18NRT, 1:10 in wt. with ethanol) dispersions were spin-coated on the as-prepared substrate with a speed of 5000 r min^{-1} and heated under conditions mentioned above. The perovskite $CH_3NH_3PbI_3$ films were prepared through the following method: first, 159 mg CH_3NH_3I, 461 mg PbI_2, and 76 mg thiourea were dissolved in 1 mL DMF at the ambient temperature. Then, the perovskite film was fabricated on the as-prepared ETL in nitrogen atmosphere. Specifically, 50 µL perovskite precursor solution was added dropwise onto the substance of FTO/TiO_2 compact layer/thin TiO_2 mesoporous layer. After the substrate was spun at 4000 r min^{-1} for at least 10 s, one drop (60 µL) of antisolvent ethyl acetate was added on the center of the substrate to facilitate quick crystallization of the perovskite. Subsequently, three more drops (150–200 µL) of ethyl acetate were added to fully cover the stationary film and kept for 60 s. The film prepared without the addition of thiourea or EA postprocessing was denoted as pristine, the film without EA postprocessing was denoted as thiourea, and the film fabricated from the thiourea-containing precursor followed by twice EA processing was denoted as thiourea-EA. The as-obtained films were annealed at 90 °C for 0.5 h. The hole transfer layer was spin-coated at 4000 r min^{-1} for 30 s. Finally, the Au electrode was fabricated by thermal evaporation. The active area was 0.12 cm^2.

Characterization: The XRD was recorded by X-ray diffractometer (PANalytical, The Netherlands) with Cu Kα radiation. The absorption and transmission spectra were measured by an UV–vis spectrophotometer (UV-3600, Shimadzu). The PL spectra and fluorescence decay curves were taken out with combined steady state and time resolved fluorescence spectrometer (FLS980, Edinburgh). The top-view morphologies of the perovskite films and the cross-section images were obtained by a high-resolution SEM (SU-8020, Hitachi). The infrared spectroscopy was measured by Fourier transform infrared spectrometry (VERTEX80v, Bruker). The photovoltaic characteristics and EIS of the devices were performed by an electrochemical workstation (Zahner, Zennium). The standard sun light (AM 1.5, 100 mW cm^{-2}) was provided by a solar simulator (SOL02 series, Crowntech). The IMVS/IMPS were also characterized on the electrochemical workstation with the assistant of light source Zahner (PP211). The IPCE spectra were measured from an accessory of Zahner electrochemical workstation.

Supporting Information

Supporting Information is available from the Wiley Online Library or from the author.

Acknowledgements

This work was supported by the "thousands talents" program for pioneer researcher and his innovation team, China. This work was also supported by the National Science Foundation of China (51374029 and 91433102), Program for New Century Excellent Talents in University (NCET-13-0668), Fundamental Research Funds for the Central Universities (FRF-TP-14-008C1), and China Postdoctoral Science Foundation (2014M550675).

Received: September 11, 2016
Revised: November 18, 2016
Published online: December 29, 2016

[1] M. A. Green, A. Ho-Baillie, H. J. Snaith, *Nat. Photonics* **2014**, *8*, 506.
[2] N.-G. Park, *Mater. Today* **2015**, *18*, 65.
[3] X. Li, D. Bi, C. Yi, J.-D. Décoppet, J. Luo, S. M. Zakeeruddin, A. Hagfeldt, M. Grätzel, *Science* **2016**, *353*, 58.
[4] C. Roldan-Carmona, P. Gratia, I. Zimmermann, G. Grancini, P. Gao, M. Graetzel, M. K. Nazeeruddin, *Energy Environ. Sci.* **2015**, *8*, 3550.
[5] J. Wei, C. Shi, Y. Zhao, W. Zhou, H. Li, R. Fu, D. Yu, Q. Zhao, *Sci. China Mater.* **2016**, *59*, 769.
[6] F. K. Aldibaja, L. Badia, E. Mas-Marza, R. S. Sanchez, E. M. Barea, I. Mora-Sero, *J. Mater. Chem. A* **2015**, *3*, 9194.
[7] W. Qiu, T. Merckx, M. Jaysankar, C. M. de la Huerta, L. Rakocevic, W. Zhang, U. W. Paetzold, R. Gehlhaar, L. Froyen, J. Poortmans, D. Cheyns, H. J. Snaith, P. Heremans, *Energy Environ. Sci.* **2016**, *9*, 484.
[8] N. J. Jeon, J. H. Noh, W. S. Yang, Y. C. Kim, S. Ryu, J. Seo, S. I. Seok, *Nature* **2015**, *517*, 476.
[9] N. K. Noel, A. Abate, S. D. Stranks, E. S. Parrott, V. M. Burlakov, A. Goriely, H. J. Snaith, *ACS Nano* **2014**, *8*, 9815.
[10] J. W. Lee, H. S. Kim, N. G. Park, *Acc. Chem. Res.* **2016**, *49*, 311.
[11] N. J. Jeon, J. H. Noh, Y. C. Kim, W. S. Yang, S. Ryu, S. Il Seol, *Nat. Mater.* **2014**, *13*, 897.
[12] W. S. Yang, J. H. Noh, N. J. Jeon, Y. C. Kim, S. Ryu, J. Seo, S. I. Seok, *Science* **2015**, *348*, 1234.
[13] Y. C. Shao, Y. J. Fang, T. Li, Q. Wang, Q. F. Dong, Y. H. Deng, Y. B. Yuan, H. T. Wei, M. Y. Wang, A. Gruverman, J. Shielda, J. S. Huang, *Energy Environ. Sci.* **2016**, *9*, 1752.
[14] T. Baikie, Y. N. Fang, J. M. Kadro, M. Schreyer, F. X. Wei, S. G. Mhaisalkar, M. Graetzel, T. J. White, *J. Mater. Chem. A* **2013**, *1*, 5628.
[15] G. C. Xing, N. Mathews, S. S. Lim, N. Yantara, X. F. Liu, D. Sabba, M. Gratzel, S. Mhaisalkar, T. C. Sum, *Nat. Mater.* **2014**, *13*, 476.
[16] S. Y. Leblebici, L. Leppert, Y. Li, S. E. Reyes-Lillo, S. Wickenburg, E. Wong, J. Lee, M. Melli, D. Ziegler, D. K. Angell, D. F. Ogletree, Paul D. Ashby, F. M. Toma, J. B. Neaton, I. D. Sharp, A. Weber-Bargioni, *Nat. Energy* **2016**, *1*, 16093.
[17] C. Fei, L. Guo, B. Li, R. Zhang, H. Fu, J. Tian, G. Cao, *Nano Energy* **2016**, *27*, 17.
[18] K. Tvingstedt, O. Malinkiewicz, A. Baumann, C. Deibel, H. J. Snaith, V. Dyakonov, H. J. Bolink, *Sci. Rep.* **2014**, *4*, 6071.
[19] D. Y. Liu, M. K. Gangishetty, T. L. Kelly, *J. Mater. Chem. A* **2014**, *2*, 19873.
[20] M. Saliba, T. Matsui, J.-Y. Seo, K. Domanski, J.-P. Correa-Baena, M. K. Nazeeruddin, S. M. Zakeeruddin, W. Tress, A. Abate, A. Hagfeldt, M. Gratzel, *Energy Environ. Sci.* **2016**, *9*, 1989.
[21] M. D. Xiao, F. Z. Huang, W. C. Huang, Y. Dkhissi, Y. Zhu, J. Etheridge, A. Gray-Weale, U. Bach, Y. B. Cheng, L. Spiccia, *Angew. Chem., Int. Ed.* **2014**, *53*, 9898.
[22] N. Ahn, D. Y. Son, I. H. Jang, S. M. Kang, M. Choi, N. G. Park, *J. Am. Chem. Soc.* **2015**, *137*, 8696.
[23] A. V. Kustov, N. L. Smirnova, M. B. Berezin, *Thermochim. Acta.* **2011**, *521*, 224.
[24] S. Y. Sun, T. Salim, N. Mathews, M. Duchamp, C. Boothroyd, G. C. Xing, T. C. Sum, Y. M. Lam, *Energy Environ. Sci.* **2014**, *7*, 399.

[25] W. Nie, H. Tsai, R. Asadpour, J.-C. Blancon, A. J. Neukirch, G. Gupta, J. J. Crochet, M. Chhowalla, S. Tretiak, M. A. Alam, H.-L. Wang, A. D. Mohite, *Science* **2015**, *347*, 522.
[26] J. P. C. Baena, L. Steier, W. Tress, M. Saliba, S. Neutzner, T. Matsui, F. Giordano, T. J. Jacobsson, A. R. S. Kandada, S. M. Zakeeruddin, A. Petrozza, A. Abate, M. K. Nazeeruddin, M. Gratzel, A. Hagfeldt, *Energy Environ. Sci.* **2015**, *8*, 2928.
[27] W. Ke, G. Fang, J. Wang, P. Qin, H. Tao, H. Lei, Q. Liu, X. Dai, X. Zhao, *ACS Appl. Mater. Interfaces* **2014**, *6*, 15959.
[28] T. Shen, J. Tian, B. Li, G. Cao, *Sci. China Mater.* **2016**, *59*, 833.
[29] X. Xu, H. Y. Zhang, J. J. Shi, J. Dong, Y. H. Luo, D. M. Li, Q. B. Meng, *J. Mater. Chem. A* **2015**, *3*, 19288.
[30] H. N. Chen, Z. H. Wei, H. X. He, X. L. Zheng, K. S. Wong, S. H. Yang, *Adv. Energy Mater.* **2016**, *6*, 1502087.
[31] X. X. Wu, M. T. Trinh, D. Niesner, H. M. Zhu, Z. Norman, J. S. Owen, O. Yaffe, B. J. Kudisch, X. Y. Zhu, *J. Am. Chem. Soc.* **2015**, *137*, 2089.
[32] P. Docampo, F. C. Hanusch, S. D. Stranks, M. Doblinger, J. M. Feckl, M. Ehrensperger, N. K. Minar, M. B. Johnston, H. J. Snaith, T. Bein, *Adv. Energy Mater.* **2014**, *4*, 1400355.
[33] Q. Tai, P. You, H. Sang, Z. Liu, C. Hu, H. L. Chan, F. Yan, *Nat. Commun.* **2016**, *7*, 11105.
[34] J. Shi, X. Xu, D. Li, Q. Meng, *Small* **2015**, *11*, 2472.
[35] A. Pockett, G. E. Eperon, T. Peltola, H. J. Snaith, A. Walker, L. M. Peter, P. J. Cameron, *J. Phys. Chem. C* **2015**, *119*, 3456.
[36] C. Tao, S. Neutzner, L. Colella, S. Marras, A. R. S. Kandada, M. Gandini, M. De Bastiani, G. Pace, L. Manna, M. Caironi, C. Bertarelli, A. Petrozza, *Energy Environ. Sci.* **2015**, *8*, 2365.
[37] E. L. Unger, E. T. Hoke, C. D. Bailie, W. H. Nguyen, A. R. Bowring, T. Heumuller, M. G. Christoforo, M. D. McGehee, *Energy Environ. Sci.* **2014**, *7*, 3690.
[38] S. Meloni, T. Moehl, W. Tress, M. Franckevicius, M. Saliba, Y. H. Lee, P. Gao, M. K. Nazeeruddin, S. M. Zakeeruddin, U. Rothlisberger, M. Graetzel, *Nat. Commun.* **2016**, *7*, 10334.
[39] J. B. You, L. Meng, T. B. Song, T. F. Guo, Y. Yang, W. H. Chang, Z. R. Hong, H. J. Chen, H. P. Zhou, Q. Chen, Y. S. Liu, N. De Marco, Y. Yang, *Nat. Nanotechnol.* **2016**, *11*, 75.
[40] J. S. Yun, J. Seidel, J. Kim, A. M. Soufiani, S. Huang, J. Lau, N. J. Jeon, S. I. Seok, M. A. Green, A. Ho-Baillie, *Adv. Energy Mater.* **2016**, *6*, 1600330.
[41] Y. Shao, Y. Yuan, J. Huang, *Nat. Energy* **2016**, *1*, 15001.
[42] Z. Zhu, Y. Bai, X. Liu, C. C. Chueh, S. Yang, A. K. Jen, *Adv. Mater.* **2016**, *28*, 6478.
[43] J. H. Kim, S. T. Williams, N. Cho, C. C. Chueh, A. K. Y. Jen, *Adv. Energy Mater.* **2015**, *5*, 1401229.
[44] L. Dou, Y. M. Yang, J. You, Z. Hong, W. H. Chang, G. Li, Y. Yang, *Nat. Commun.* **2014**, *5*, 5404.
[45] T. Kirchartz, F. Deledalle, P. S. Tuladhar, J. R. Durrant, J. Nelson, *J. Phys. Chem. Lett.* **2013**, *4*, 2371.
[46] M. Bernechea, N. C. Miller, G. Xercavins, D. So, A. Stavrinadis, G. Konstantatos, *Nat. Photonics* **2016**, *10*, 521.